Unraveling the physics of the Yellowstone magmatic system using geodynamic simulations

Georg S. Reuber,[1] Boris J.P. Kaus,[1,2,3] Anton A. Popov,[1] and Tobias S. Baumann[1]

[1] *Institute of Geosciences, Johannes Gutenberg-University, Mainz, Germany*
[2] *Center for Computational Sciences Mainz, Johannes Gutenberg-University, Mainz, Germany*
[3] *Volcanoes, Atmospheres and Magmatic Open Systems (VAMOS) research center, Johannes Gutenberg-University, Mainz, Germany*

The Yellowstone magmatic system is one of the largest magmatic systems on Earth, and thus an ideal location to study magmatic processes. Whereas previous seismic tomography results could only image a shallow magma chamber, a recent study using more seismometers showed that a second and massive partially molten mush chamber exists above the Moho [1]. To understand the mechanics of this system, it is thus important to take the whole system from the mantle plume up to the shallow magma chambers into account.

Here, we employ lithospheric-scale 3D visco-elasto-plastic geodynamic models to test the influence of parameters such as the connectivity of the chambers and rheology of the lithosphere on the dynamics of the system. A gravity inversion is used to constrain the effective density of the magma chambers, and an adjoint modelling approach reveals the key model parameters affecting the surface velocity.

Model results show that a combination of connected chambers with plastic rheology can explain the recorded slow vertical surface uplift rates of around 1.2 cm/a, as representing a long term background signal. A geodynamic inversion to fit the model to observed GPS surface velocities, reveals that the magnitude of surface uplift varies strongly with the viscosity difference between the chambers and the crust. Even though stress directions have not been used as inversion parameter, modelled stress orientations are consistent with observations.

However, phases of larger uplift velocities can also result from magma inflation which is a short term effect. We consider two approaches: 1) overpressure in the magma chamber in the asthenosphere and 2) inflation of the uppermost chamber prescribed by an internal kinematic boundary condition. We demonstrate that the asthenosphere inflation has a smaller effect on the surface velocoties in comparison with the uppermost chamber inflation. We show that the pure buoyant uplift of magma bodies in combination with magma inflation can explain (varying) observed uplift rates at the example of the Yellowstone volcanic system.

Keywords: Yellowstone, 3D modeling, inversion, adjoint, overpressure

I. INTRODUCTION

Understanding magmatic systems has been a long-standing research topic within the solid-Earth geosciences. To understand the underlying processes better several volcanic areas on the Earth have been geophysically monitored, geologically mapped and interpreted. At the same time numerical or analog models have been developed to unravel the mechanical driving forces. As a result, a paradigm shift has happened over the last decade, and we now know that magmatic systems are lithospheric-scale systems composed by many smaller pulses of melt [2]. Yet, our understanding of the physics of such systems remains somewhat limited.

Classically, models have been used to link surface deformation data to the depth, size and overpressure of a magma chamber. If the rocks are elastic and the magma chamber is spherical and embedded in an infinite half-space, an analytical solution exist [3]. This approach has been widely applied, for example, to show that surface uplift above the Hekla volcano (Iceland) is consistent with a reservoir at 8 km depth [4], to constrain the depth of the magma source beneath Etna [5], or to reproduce cyclicity in ground deformation at Montserrat as a result of pressurization of a dike-conduit system [6]. The Mogi approach has been extended to account for topographic effects and crustal heterogeneities in both 2D [e.g., 7]) and 3D [e.g., 8]). Furthermore, the analytical solution has been extended to include viscous effects, for example by [9], who compare the temperature-dependent visco-elastic to the elastic solution and show that the required overpressures to fit observed uplift at Etna is about a third lower in the visco-elastic case, which is more consistent with the lithospheric stress state. Such overpressures may nevertheless exceed the yield strength of crustal host rocks, in which case the material deforms plastically rather than (visco-)elastic. An evaluation of such elasto-plastic effects shows that this produces higher uplift rates for the same overpressure [10, 11]. [12] argue that at Hawaii, this will likely result in fracturing of the host rock around the magma chamber and result in a net of pathways, which is inconsistent with a spherical source of overpressure. [13] also point out the limitations of the assumption that magmatic bodies are spherical, and show that whereas uplift rates can often be reproduced with a spherical models, the resulting depth of the source is incorrect.

Many of these previous studies focus on upper-crustal

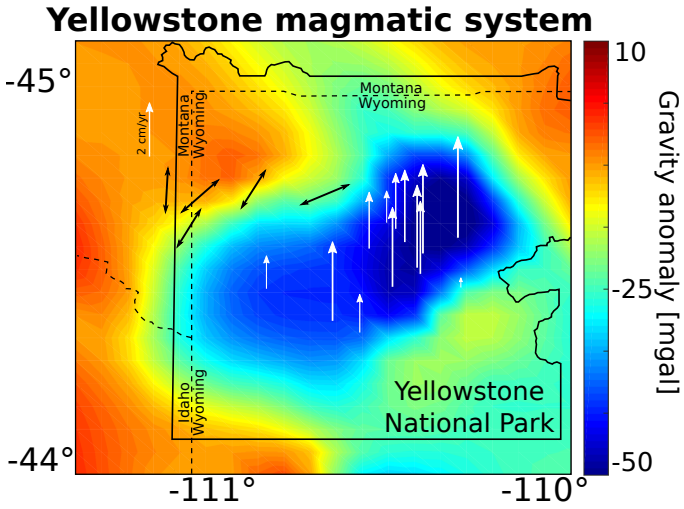

FIG. 1. Overview of some geophysical data for Yellowstone used in this work. The area corresponds to the computational domain presented in this work. Colors indicate the bouguer gravity anomaly in the area referenced to the anomaly close to the boundary of the area. Data is taken from the online archive of the Pan American Center for Earth and Environmental Sciences (PACES) and [50]. White vertical arrows indicate the GPS velocities during a period of high activity from 2003 to 2008 [20]. Black arrows represent the orientation of the minimum principal stress (σ_3) (taken from [21] and references therein).

magma chambers and consider a single pulse of magma. Yet, as magmatic systems are likely formed by many pulses, it is important to take those into account, as done by [14] who investigate the effect of pulses on the style and frequency of eruptions and provide scaling laws for mechanical locking of the magma chamber due to thermal cooling. The work by [15] and [16] demonstrates that subsequent magmatic pulses help keep the system hot and partially molten, which may significantly change the mechanics of magma transport once a critical amount of heating has occured [17].

Seismic tomography studies of magmatic systems give important insights into the 3D structure at depth. Yet, interpreting these results in terms of melt content with depth is not straightforward as the seismic wavelengths themselves are several kilometers in size and the distribution of seismometers is often sub-optimal. Some attempts have been made to perform a joint inversion in which thermal models and melting parameterizations are combined with tomographic inversions. Results for Montserrat show that melt fractions obtained in this manner are substantially larger than those directly inferred from interpreting seismic data [18]. Yet, whereas this gives important new insights in the geometry of the system, it does not tell much about the physics of magmatic systems, which is the focus of our work.

We use the Yellowstone magmatic system (Wyoming, US) as a case study, as it is one of the best studied volcanic systems on Earth that has a significant hazard potential having ejected around 1000 km^3 during the last eruption. Even though there are no indications that an eruption of this size is imminent, if it occurs it will likely have significant effects on the global economy. A comprehensive summary on the evolution and petrology of the Yellowstone magmatic system is given by [19]. Geophysically, Yellowstone is a well-studied area. Figure 1 summarizes the available observational data constraints that include gravity anomaly, GPS uplift velocities for a period of high activity from 2003 to 2008 [20], and the orientation of the minimum principal stress ([21]). Furthermore, [22] and [23] give an overview over the seismic tomography, earthquakes, surface uplift and stress orientations within and at the system. Even though the exact geometry of the Yellowstone magmatic system remains under discussion, recent publications, (e.g. [1] based on seismic tomography), suggest that the system extends over lithospheric scales ranging from a deep mantle plume over a large partially molten magma chamber within the lower crust to a shallow partially molten magma chamber in the upper crust. We make use of these tomographic results and convert the velocity anomalies into a 3D geometry of the magma chambers as part of our numerical models. We subsequently perform 3D mechanical models of the system, taking the visco-elasto-plastic rheology of rocks into account and compare model predictions with data.

Recently, it was shown that geodynamic inversion frameworks can serve as a powerful tool to link geophysical observations with thermo-mechanically consistent deformation models to infer rheological properties of the crust and lithosphere [24, 25]. Here, we apply a gradient-based adjoint inversion technique combined with data assimilation [26] to constrain the dynamics of the Yellowstone magmatic system, and discuss whether full 3D models are required for such systems, or 2D models are sufficient. In the following sections we describe the underlying numerical method [27], the adjoint inversion framework, and provide some background on the thermodynamical modeling that is incorporated in this study. We present two different approaches to simulate the effect of inflation of a crustal magma chamber, while simultaneously taking the buoyancy effect of the lithospheric-scale magmatic system into account. We systematically test the effect of rheological complexities on surface uplift and incorporate the most successful of these models in an inversion approach to constrain the material parameters from data.

II. METHODS

A. Physics and numerics

In this work we solve for the conservation of momentum and mass in a compressible formulation. For a domain Ω with a boundary $\partial\Omega$ the underlying coupled equa-

tion system is given by:

$$\frac{\partial \tau_{ij}}{\partial x_j} - \frac{\partial P}{\partial x_i} + \rho g_i = 0, \tag{1}$$

$$\frac{1}{K}\frac{DP}{Dt} + \frac{\partial v_i}{\partial x_i} = 0. \tag{2}$$

Here $x_i (i = 1, 2, 3)$ denotes Cartesian coordinates, v_i is the velocity vector, P is the pressure, τ_{ij} is the Cauchy deviator stress tensor, ρ is the density, g_i is the gravity acceleration vector, K is the elastic bulk modulus, and D/Dt stands for the material time derivative. Here and below we imply the Einstein summation convention. Due to a moderate time span of the models considered in this work ($\sim 10^4$ years), we ignore the effect of temperature advection and diffusion, and therefore omit the solution of the energy balance equation. On a free-slip boundary with a normal vector pointing in i-th direction we enforce the following condition:

$$v_i = \overline{v}, \quad \frac{\partial v_j}{\partial x_i} = 0, \quad j \neq i, \tag{3}$$

where $\overline{v}$ is the normal velocity component. On a no-slip boundary we apply $v_i = 0$.
The deviatoric stress tensor is defined by a set of visco-elasto-plastic constitutive equations of the form:

$$\dot{\varepsilon}_{ij} = \dot{\varepsilon}^{el}_{ij} + \dot{\varepsilon}^{vs}_{ij} + \dot{\varepsilon}^{pl}_{ij} = \frac{\overset{\diamond}{\tau}_{ij}}{2G} + \frac{\tau_{ij}}{2\eta} + \dot{\gamma}\frac{\partial Q}{\partial \tau_{ij}}, \tag{4}$$

$$\dot{\varepsilon}_{ij} = \frac{1}{2}\left(\frac{\partial v_i}{\partial x_j} + \frac{\partial v_j}{\partial x_i}\right) - \frac{1}{3}\frac{\partial v_k}{\partial x_k}\delta_{ij}, \tag{5}$$

$$\overset{\diamond}{\tau}_{ij} = \frac{\partial \tau_{ij}}{\partial t} + \tau_{ik}\omega_{kj} - \omega_{ik}\tau_{kj}, \tag{6}$$

$$\omega_{ij} = \frac{1}{2}\left(\frac{\partial v_i}{\partial x_j} - \frac{\partial v_j}{\partial x_i}\right), \tag{7}$$

where $\dot{\varepsilon}_{ij}$ is the total deviatoric strain rate tensor, δ_{ij} is the Kronecker delta, the superscripts el, vs, and pl correspond to elastic, viscous, and plastic strain rate components, respectively, G is the elastic shear modulus, $\overset{\diamond}{\tau}_{ij}$ is the Jaumann objective stress rate, ω_{ij} is the spin tensor, η is the creep viscosity, $\dot{\gamma}$ is the magnitude of plastic strain rate (plastic multiplier), and Q is the plastic potential function. The effective viscosity is defined as a function of temperature, and strain-rate according to the dislocation creep mechanism [e.g., 28]:

$$\eta = \frac{1}{2}\left(B_n\right)^{-\frac{1}{n}}\left(\dot{\varepsilon}_{II}\right)^{\frac{1}{n}-1}\exp\left(\frac{E_n}{nRT}\right). \tag{8}$$

In the above expression, $\dot{\varepsilon}_{II} = \left(\frac{1}{2}\dot{\varepsilon}_{ij}\dot{\varepsilon}_{ij}\right)^{1/2}$ denotes the effective strain rate measure (square root of the second invariant), n is the stress exponent of the dislocation creep, and B_n, E_n, are the creep constant, and activation energy, respectively, R is the gas constant and T is temperature.

The magnitude of plastic multiplier is determined by enforcing the Drucker-Prager failure criterion [29], given by:

$$F = \tau_{II} - \sin(\phi)\, P - \cos(\phi)\, C \leq 0, \tag{9}$$

where $\tau_{II} = \left(\frac{1}{2}\tau_{ij}\tau_{ij}\right)^{1/2}$ is the effective deviatoric stress, ϕ is the friction angle, and C is the cohesion. To prevent the non-symmetry in the Jacobian matrix required by the adjoint method (see section II B) we use the lithostatic, instead of the fully dynamic pressure in the equation (9) in the simulations presented here. In this work we do not consider the effect of strain softening on the friction and cohesion parameters. We adopt the dilatation-free non-associative Prandtl-Reuss flow rule, defined by the following plastic potential function:

$$Q = \tau_{II} \tag{10}$$

The dependence of the density field on the pressure, temperature, and melt fraction is assumed to be given by a phase diagram (see section II C). The computation is performed externally using the consistent thermodynamic modeling with Perple_X. The feedback between density and influencing parameters is updated every nonlinear iteration.

We discretize and solve a coupled set of conservation and constitutive equations using 3D thermo-mechanical code LaMEM [27], which is based on a staggered finite differences approximation [e.g., 30–32]. The material properties are advected using a marker-and-cell method [30]. To guarantee the computational stability for a large time step we employ a stabilized free surface boundary condition using the sticky-air approach [33, 34]. Nonlinearities are handled by a preconditioned Jacobian-Free Newton-Krylov (JFNK) method with line-search as implemented in the PETSc SNES nonlinear solver framework [35]. The gravity anomaly computation adopted in LaMEM is based on a rectangular prism approximation [e.g., 36, 37]. Further information regarding the computational efficiency of LaMEM, and the computational infrastructure used to compute the models is given in Appendix 1.

B. Adjoint equations

The adjoint method for solving inverse problems is a powerful tool [e.g. 38]. It is essentially based on a gradient-based inversion approach such as BFGS (Broyden-Fletcher-Goldfarb-Shanno) Quasi-Newton method [e.g., 26]. The gradients of the cost function with respect to model parameters are computed using an efficient (adjoint) procedure. The adjoint gradients computation can be summarized as follows:

$$\psi = \left(\boldsymbol{J}^T\right)^{-1}\left(\frac{\partial F}{\partial \boldsymbol{x}}\right)^T, \tag{11}$$

$$\frac{dF}{d\boldsymbol{p}} = -\psi^T\frac{\partial \boldsymbol{r}}{\partial \boldsymbol{p}}, \tag{12}$$

where $\boldsymbol{p}$ is the model parameter vector, e.g. densities, viscosities, etc., $\boldsymbol{J} = \partial \boldsymbol{r}/\partial \boldsymbol{x}$ is the Jacobian matrix of the forward problem, namely the derivative of the residual ($\boldsymbol{r}$) with respect the solution vector ($\boldsymbol{x}$), F is the objective (cost) function, quantifying the misfit between the observations and simulation results. The partial derivatives $\partial \boldsymbol{r}/\partial \boldsymbol{p}$ might be difficult to compute analytically. In these cases they can be approximated by finite differences. Numerical codes that solve the nonlinear equations by a Newton-Raphson method usually have the Jacobian matrix readily available. The adjoint gradient computation procedure can be rendered efficient since it only involves a single linear solve irrespective of the number of gradients.

The adjoint gradients can be used not only to solve the inverse problem but also to quantify the influence of model parameters on the model solution, i.e. to construct a scaling law [39]. The essence of the adjoint scaling law can be briefly summarized as follows. We start with redefining the cost function (F) to be an arbitrary solution parameter of the forward model, e.g. (non-dimensional) velocity, instead of the misfit between the model and observation. Next, we assume that the actual scaling law for the solution parameter (F) can be approximated by the following multiplicative from:

$$F \approx A_F \, p_1^{b_1} \, p_2^{b_2} \ldots p_n^{b_n}, \tag{13}$$

where A_F is the dimensionally-consistent prefactor. We can now conveniently compute the scaling exponents (b_i) of the approximate scaling law using the following expressions:

$$b_i = \frac{dF}{dp_i} \frac{p_i}{F}. \tag{14}$$

Here we use adjoint gradient procedure (equations 11 - 12) to estimate the derivatives of the solution parameter (F) with respect to models parameters ($\boldsymbol{p}$).

C. Thermodynamic modeling

To create a thermodynamically consistent model of the Yellowstone magmatic system, we use the thermodynamic modeling tool Perple_X [40], version 6.7.4. Perple_X is freely available software which ensures the reproducibility of the results shown in this work. Furthermore, Perple_X has already proven its applicability to the field of thermomechanical modeling in multiple publications [e.g 41–44]. By Gibbs free energy minimization Perple_X computes material properties including phase changes. Here, we use it to compute rock densities as functions of pressure and temperature. The calculations were performed using the database of Holland and Powell [45]. As an approximation for the crust surrounding the Yellowstone magmatic chambers we take the average crust compositions from [46], described in table I.

To generate an initial guess for the effective densities of the magma chambers we used the method described in [47] for the whole rock data analysis described by [19]. The used rock composition is shown in table I. In the gravity inversion, we vary the density between the completely molten and solid end-members to find a fit to the gravity signal.

TABLE I. Major element composition (in weight percent oxide) for all rock types used in this work.

Oxide	Rhyolite	Upper crust	Basalt	Lower crust
SIO_2	72.29	66.62	49.51	53.40
TIO_2	0.16	0.64	2.28	0.82
AL_2O_3	13.40	15.40	15.96	16.90
FEO	0.00	5.04	9.00	8.57
MNO	0.04	0.10	0.18	0.10
MGO	0.20	2.48	6.27	7.24
CAO	0.85	3.59	9.79	9.59
NA_2O	2.77	3.27	2.69	2.65
K_2O	5.40	2.80	0.57	0.61
H_2O	1.82	3.00	1.00	1.50

References: [46], [19]

III. MODEL SETUP AND DATA INTEGRATION

The seismic study of [1] represents the most recent seismic tomography model of the Yellowstone magmatic system, including a mantle plume and two distinct magma chambers in the lower and upper crust, respectively. We make use of their interpretation of the velocity anomalies and construct a 3D geometry of the magma chambers by digitizing the horizontal and vertical cross sections from [1]. The geometry on the horizontal and vertical sections was subsequently turned into a 3D model using the freely available software package geomIO [48]. The computational domain includes the entire Yellowstone national park and the eastern part of Idaho, which is roughly 110 km in East-West and 120 km in North-South direction, respectively (see figure 2). The depth of the domain is restricted to 90 km, combined with an internal free surface at 0 km, overlain by a 10 km thick free-air layer [49]. The numerical resolution is $128 \times 128 \times 256$ nodes in x, y and z direction. All boundaries are treated as free slip.

The first two kilometers of the domain consist of a sediment layer, followed by 12 km of upper crust including the shallow magma chamber. The lower crust includes the lower magma chamber and extends 36 km in the vertical direction. The bottom of the domain is defined by the mantle lithosphere until a depth of 70 km and followed by asthenosphere. A connection of the mantle plume to the lower boundary simulates the connection to the deeper mantle. Additionally, connection channels are added to the model setup between the plume and the chambers, which can be activated to simulate weak connective areas, comparable to diking areas. Inflation of the magma chambers from the deeper mantle can be sim-

TABLE II. Material properties used in this work. All phases with constant density have a thermal expansion coefficient, α of 3×10^{-5} K^{-1}. All phases except the free-air phase are defined by a constant thermal conductivity (k) of 3 W/(mK) and a heat capacity (cp) of 1000 J/(kgK). All phases except the free-air phase are defined by a constant cohesion (C) of 1 MPa and a friction angle of 30 °. All phases except the free-air phase have a poison ratio of 0.3. The magma chamber viscosities are constant. The rheological flow laws for the viscosities are taken from [55]: Wet Quartzite $A_n = 3.2\times10^{-4}$ MPa^{-n}/s, $n = 2.3$, $E_n = 154$ kJ/(MPa mol), $V_n = 0$ m^3/mol; Quartzite $A_n = 6.7\times10^{-6}$ MPa^{-n}/s, $n = 2.4$, $E_n = 156$ kJ/(MPa mol), $V_n = 0$ m^3/mol; Plagioclase (An75) $A_n = 3.3\times10^{-4}$ MPa^{-n}/s, $n = 3.2$, $E_n = 238$ kJ/(MPa mol), $V_n = 0$ m^3/mol; Dry Olivine $A_n = 2.5\times10^{-4}$ MPa^{-n}/s, $n = 3.5$, $E_n = 532$ kJ/(MPa mol), $V_n = 17\times10^{-6}$ m^3/mol. Other parameters are taken from [37].

Phase	Density [kg/m^3]	Viscosity [Pas]	Shear modulus (G) [GPa]
Free-Air	1	10^{19}	none
Sediment	2500	Wet Quartzite	50
Upper crust	phase diagram	Quartzite	50
Lower crust	phase diagram	Plagioclase (An75)	50
Lithosphere	3400	Dry Olivine	50
Asthenosphere	3400	Dry Olivine	50
Upper chamber	2519	$10^{19}/10^{21}$	50
Lower chamber	2660	$10^{19}/10^{21}$	50
Mantle plume	3060	10^{19}	50

ulated by applying an overpressure at the lower bottom in the region of this connection. Alternatively, simultaneous deflation and inflation of the chambers in the lower and upper crust, respectively, can be simulated by activating a kinematic internal boundary condition between the chambers.

The temperature structure consists of three linear geotherms. In the sediment and the upper crust the geotherm is 15 K/km, followed by 3 K/km in the lower crust and lithosphere and 0.5 K/km for the rest of the domain. The surface temperature is assumed to be 0°C. The initial setup is shown in figure 2, while the employed material properties of all phases/rocktypes are summarized in table II.

IV. INVERSE MODELING APPROACH

For the inversions, we assume that the overall large-scale geometry of the Yellowstone magmatic system does not change, particularly with respect to the shape of the chambers and the structure of the layers. Since the buoyancy force is a major driving force controlling surface uplift, we will first constrain the density structure of the model by fitting the gravity anomaly (figure 1). We change the effective densities of the two chambers, while keeping the densities of the surrounding crusts fixed (and computed from phase diagrams). The melt content of the mush chambers influences the effective density of the chambers. In this work we will not investigate the exact

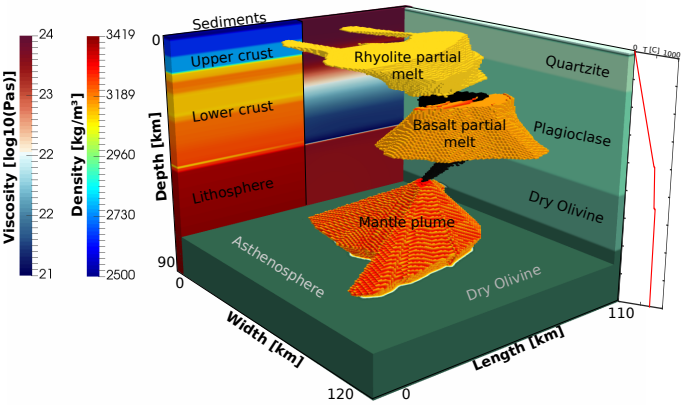

FIG. 2. Model setup of the computational domain representing the lithospheric scale Yellowstone magmatic system. The positions and shapes of the phases are inspired by the seismic tomography data shown in [1]. Chambers and mantle plume are connected, while these connections can be active or made inactive (by giving it the same material properties as the host rock). Colors at the back of the domain show the density and viscosities at this location, while temperature along a 1D profile through the middle of the domain is shown at the right.

amount of melt in the magma chambers but rather invert directly for the effective density difference between the chamber and surrounding rocks, as this is the key parameter that controls gravity anomalies. If the density of the melt and that of the solid rock within the mush chamber is known, we can retrieve melt content from it [e.g., 47]. In doing this, we make the implicit assumption that the melt content within each of the partially molten chambers in our model setup is constant. In nature, it is quite possible that the melt content within the chambers varies as well, and our approach should thus be considered to only catch the first order effects on both the gravity field and the dynamics of the system. Gravity anomalies are well known to be non-unique with respect to the relative density and geometry of the anomaly. [24] showed that using a joint geodynamic inversion of surface velocities and gravity data reduces the ambiguities of the inverse problem, that is why we additionally perform an inversion for the surface velocities through changing the viscosities of the layers. For the gravity inversion, we compute the misfit between the data and the simulation at each parameter combination. Our reference gravity field is based on the density profile at a vertical boundary of the domain, excluding magma chambers and the mantle plume. The only free parameters in this setup are the effective densities of the two chambers, which makes it a computationally efficient problem permitting a grid search inversion.

To obtain a good starting guess for the velocity inversion, we first compute the sensitivities of the surface velocities to the changes in material parameters, and identify those of them that have biggest influence on the results. This is accomplished by computing and comparing

the adjoint scaling exponents for each material parameter as described in section (II B). We found that there are 8 parameters that are crucial, and we therefore restricted our inversion to these ones.

The actual inversion for the surface velocities combines the adjoint gradients with gradient descent inversion framework that includes a line search algorithm. The gradient-based inversions (in contrast to e.g. grid search) are characterized by inability to map all parameter combinations, but instead follow the gradient towards the next (local) best fit. The advantage is that it makes the inversions computationally tractable, but the disadvantage is that it is not guaranteed to converge to the global minimum.

V. RESULTS

A. 2D versus 3D

Since 3D simulations are computationally more expensive than 2D ones, it is advantageous to know whether substantial part of the inversions can be done in 2D. To address this, we take two cross-sections from our 3D model along profiles shown in figure 3, and perform simulations with identical parameters as the corresponding 3D simulation. As the comparison of vertical surface velocities shows, there is a significant difference between 2D and 3D results.

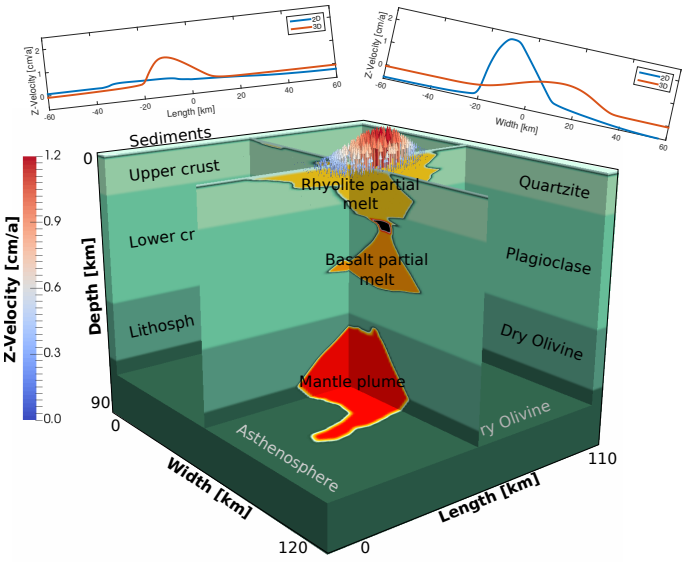

FIG. 3. Result of the comparison between 2D and 3D models. Two cross sections are shown with their respective surface velocity in 2D or 3D. The velocity profile is very distinct, suggesting that 3D effects are important to take into account.

This thus suggest that it is important to take 3D effects into account, particularly if model predictions are to be directly compared with data. The reason for the discrepancy is two-fold. On one hand, 2D simulations effectively treat magma chambers as an infinitely long cylinders, which will overestimate the available buoyancy in the system. On the other hand, three-dimensional connections between the magma chambers, as are present in our 3D setup, may not be sampled in a 2D model depending on where the cross-section was taken. This effect is present in the left cross-section in figure 3, which has the result that the 2D simulation sees the two magma chambers as being unconnected whereas they are actually connected in 3D. This explains why the 2D velocities are significantly smaller in this setup, whereas they are larger in the rightmost cross-section where the connection between the chambers is sampled in the 2D models. We therefore only employ 3D models in the remainder of this work.

B. Gravity anomaly inversion

Before performing actual geodynamic simulations, we first derive a density structure of the magma chambers of the Yellowstone magmatic system, as gravity anomaly computations are computationally much faster than geodynamic simulations. We implement the gravity computation as described in [37]. As comparison we use the compiled Bouguer anomaly data of [50] (online archive of the Pan American Center for Earth and Environmental Sciences (PACES), shown in figure 1), who performed a 2D inversion for the density structure.

By varying the effective density of the two magma chambers, we invert for the 3D density structure. We vary the effective densities from 2340 kg/m^3 to 2690 kg/m^3 for the upper and from 2590 kg/m^3 to 2730 kg/m^3 for the lower chamber, consistent with the effective density values resulting from the parametrization of [47] for the major elements found by [19], also shown in table I. Four end member cases are considered:

1. Grid search inversion: In this case, the gravity anomaly is fitted by varying the effective densities of the chambers as a whole, as shown in figure 4A (data), C (simulation result), D (mapped misfit function) and E (representative 2D cross section). Results show that we obtain an overall good fit to the data, with deviations of around 5-10 mGal (see figure 4E). There is a trade-off between the two densities (figure 4D). As expected, the gravity anomaly is more sensitive to the density of the shallower magma chamber. The final result has a density of 2496 kg/m^3 in the upper chamber, and a density of 2684 kg/m^3 for the lower chamber.

2. Heterogeneous magma chambers: We present a hand-made fit based on the result of the grid search inversion to the gravity anomaly in which we include smaller areas within the chambers that are allowed to have a higher or lower densities. As starting point, the best fit from approach 1) was

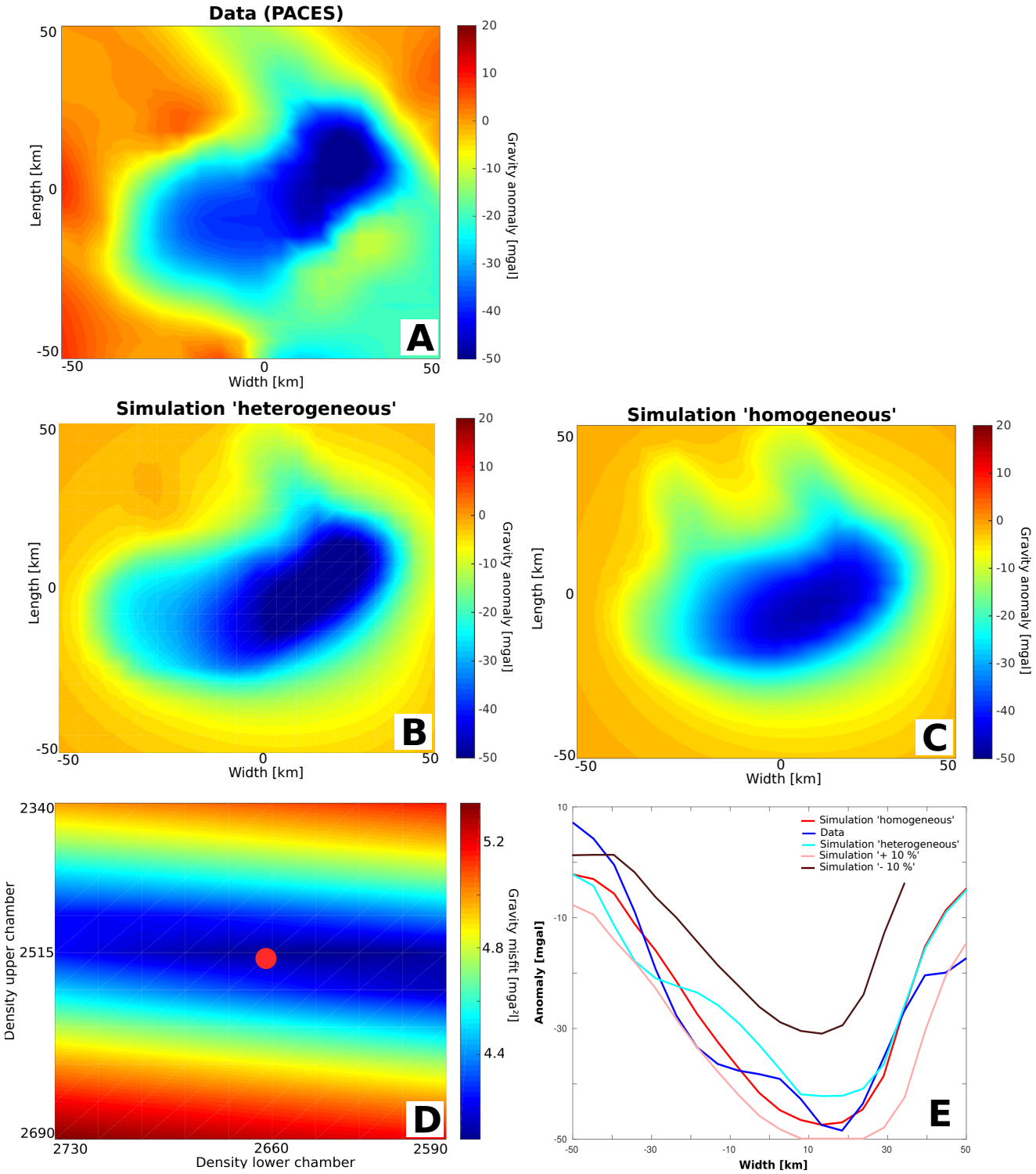

FIG. 4. Result of the gravity inversion. A: Observed gravity anomaly data from PACES. B: Best manual fit assuming heterogeneous magma chamber densities. C: Best fit model by grid search inversion, keeping the density of the chambers homogeneous. D: Misfit function in the grid search inversion. The color represents the least square misfit between the simulation and data, with blue colors indicating a good fit to the data. E: Gravity anomaly comparison between simulation result and data at a representative 1D line across the surface (along length = 0 km).

used. The result is shown in figure 4B and E. In particular, a denser heterogeneity (slightly denser than the surrounding crust) within the north east part of the chamber removed the anomalous perturbation in the gravity signal. Furthermore, the center of the magma chamber was divided in a slightly denser part in the west and a less dense part in the east. As a result the misfit is reduced in some areas, and increases in others. Doing a better fit would potentially be possible if we allow for a full, laterally varying, density structure. Given the above-described non-uniqueness of the gravity problem it is however unclear whether this will give significant new insights in the dynamics of the system, while increasing the model parameters significantly.

3. Slightly larger chambers: Since the geometry is inspired by the seismic tomography data, which includes a regularisation as part of the inversion, there is still significant room for interpretation regarding the chamber size (which we constrained using the shape of the seismic velocity contour lines). To investigate this effect, we performed simulations with 10 % larger chambers, which significantly overdetermines the gravity signal, shown in figure 4E.

4. Slightly smaller chambers: Similarly, a reduction of the volume of the chambers by 10 %, while using the same density difference between chamber and host rock, significantly underestimates the gravity signal, as shown in figure 4E.

Based on these results, we use the best-fit density structure of the grid search inversion in the remainder of this work. This assumes a density difference between upper chamber and surrounding upper crust of around 100 kg/m^3, independent of how this density difference is achieved. The density difference between the lower chamber and lower crust has a smaller effect on the gravity signal, as can be seen in figure 4D.

C. Forward modeling

In the next step, we perform 3D visco-elasto-plastic compressible geodynamic simulations. Since we are mainly interested in the present-day deformation of the lithosphere, we need to run the simulations for a few time steps until stresses have elastically build-up and do not change significantly with time after which we evaluate the simulation (see Appendix 2 for additional details).

In our simulations, the long term surface uplift is driven by the buoyancy force, caused by the density difference between chambers and crust or plume and mantle, respectively, and is inverse proportional to the effective viscosity of the layers. In addition, magma pulses may further inflate a magma chamber and induce a surface signal. We model this by either activating an over-pressure lower boundary condition, or by a kinematic internal boundary condition, as explained later. Both conditions are activated only after a steady-state stress state has been achieved in the models, which is why these simulations take both the long-term geodynamic effects and the shorter-lived magmatic pulse into account. In the following, we discuss the impact of several end member simulations.

1. No connections, visco-elastic

In phases of tectonic quietness, the partially molten magma chambers act as buoyant bodies emplaced in a tectonically quiet and elastically loaded crust. We tested this by performing a model with unconnected chambers and a visco-elastic crust without taking plasticity (generation of faults or weak zones in the crust) into account. Maximum surface velocities are on the order of 0.2 cm/a, shown in figure 5A. Furthermore, significant deviatoric stress occur between the chambers of up to 120 MPa, which suggests that it is likely that brittle failure would actually occur in these places and connect the chambers.

2. Connections, visco-elastic

In a next test, we therefore inserted a connection between the chambers in the models (as shown in figure 5B). This increased the maximum surface uplift velocities of up to 0.8 cm/a, which is in the consistent with the lower bound of the observed uplift velocities in Yellowstone, recorded during phases of low activity [e.g. 20, 51, 52].

3. Connections, visco-elasto-plastic

The crust above large scale volcanic systems is faulted in many places [e.g., 53]. For rocks, a first order representation of the stress at which they yield is given by Byerlee's law which can be numerically mimicked by a Drucker-Prager frictional plasticity law [29]. Numerical simulations that implement this will limit the stresses to remain below or at the yield stress. To understand the effect of this on the large-scale dynamics of the system we performed a simulation in which plasticity was activated (with a friction angle of 30°, and a cohesion of 1 MPa). The results show that plastic yielding is predominantly active above the magma chambers. As it effectively weakens the crust, it results in higher surface velocities of up to 1.2 cm/a (figure 5C). To give a better feeling of the overall velocity field within the system we created a movie consisting of passively advected markers. The movie is given in the online supplement and is described in Appendix 4.

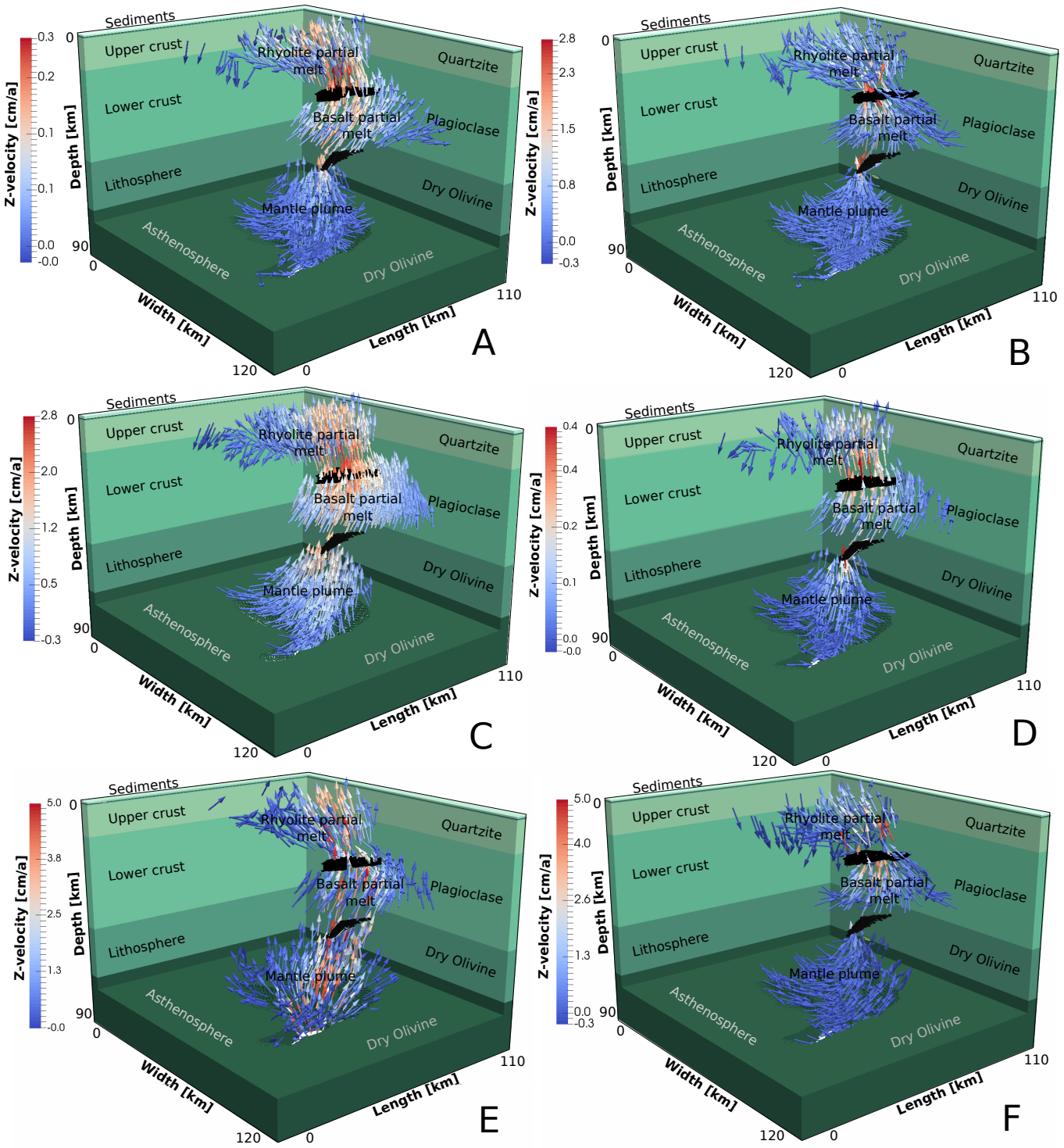

FIG. 5. Summary of the velocity structure of different end member simulations. A: No connection between the chambers and no plasticity. Maximum vertical velocities at the surface are 0.2 cm/yr. B: Connections between the chambers and no plasticity. Maximum vertical velocities at the surface are 0.8 cm/yr. C: Connections between the chambers and plasticity. Maximum vertical velocities at the surface are 1.2 cm/yr. D: Connections between the chambers, plasticity and a higher viscosity of the chambers of 10^{21} Pas, implying a lower melt content. The maximum vertical velocity at the surface is 0.2 cm/yr. E: Case with slightly larger connections between the chambers, plasticity and a basal boundary overpressure of 50 MPa. Maximum vertical velocity at the surface is 2.4 cm/yr. F: Case with a prescribed kinematic boundary condition between the chambers to simulate influx from the middle to the upper chamber of around 8 cm/a. Maximum vertical velocity at the surface is 2 cm/yr.

4. Connections, visco-elasto-plastic, less melt

So far, our models considered the partially molten viscous chambers to have a uniform and low viscosity of 10^{19} Pas, which implicitly implies that the melt content is sufficiently large to weaken the effective viscosity of the chambers to this amount (from an effective solid rock viscosity of $10^{23} - 10^{24}$ Pas). Yet, seismic tomography results suggests that the melt fraction in the upper chamber may be no more than 10% and even less in the deeper chamber [1]. Whereas it is unclear how robust these findings are, given the km-scale wavelength of seismic waves and the dampening used in seismic tomography inversions, it is at least feasible that the effective viscosity is larger than we assumed. We therefore performed an additional simulation in which the viscosity of the magma chambers was increased by two orders of magnitudes. Results show that this reduces the maximum surface velocities by a factor 6 from 1.2 to 0.2 cm/a (figure 5D). This thus suggests that the viscosity of the partially molten chambers does play an important role for the surface velocities, and that this is not solely affected by the rheology of the host rocks.

5. Connections, visco-elasto-plastic, mantle influx

In volcanology, uplift rates of volcanoes are often interpreted by comparing them with predictions of analytical or numerical models that consider a (spherical) magma chamber that is emplaced at a given depth and has a certain amount of overpressure applied at its boundary. Physically, this approach mimics the inflation of a magma chamber after the addition of new batch of magma, and if this magma chamber is embedded in a compressible elastic host rock, it will deform both the host rocks and the free surface [e.g 11, 13]. In numerical codes, this is typically done by treating the magma chamber itself as a boundary condition, which can be benchmarked versus the elastic Mogi solution [3] or a visco-elastic variation of it [9]. Whereas this approach is certainly applicable to address deformation within the shallow crust beneath a volcano, there are a number of problems of employing it to the whole lithosphere. The first issue is related to where the magma pulse comes from. In Yellowstone, magma in the upper chamber may either come from the mantle plume (an influx condition in our setup), or from extraction of melt from the lower chamber, which would result in both inflation in the upper crust and deflation in the lower crust. We consider both scenarios.

The first scenario assumes that additional magma in the upper crust comes from a new pulse of magma in the asthenosphere. The usual way of implementing this in numerical models, by setting an internal pressure boundary condition, has the disadvantage that it effectively eliminates the background lithospheric uplift rate, caused by the density difference between the magma chamber and the host rocks. This thus implies that such models only consider the effect of overpressure on deformation. An alternative approach, which we follow here, is to apply an overpressure condition at the lower boundary of the model, which propagates through the system and causes an inflation of the upper chamber, as long as it is connected to the lower boundary through weak zones. This has the advantage that it mimics more closely what happens in nature and allows for more complex partially molten regions, while at the same time taking the buoyancy effect of the chambers into account. To test whether this approach works, we benchmarked our implementation with the Del Negro viscoelastic benchmark (Appendix 3).

To test the effect of mantle magma influx on the Yellowstone model configuration, we applied an additional constant overpressure of 50 MPa at the intersection between the mantle plume and the lower boundary. Results show that this significantly increases the velocities within the mantle plume, while only resulting in slightly larger surface velocities (figure 5E). The effectiveness with which the overpressure influences the surface velocity scales with the size of the weak connection zones between the chambers. Small connections result in a significant increases of the velocity field within the mantle plume, of which only a small amount is transferred to the surface. Increasing the size of the connections, increases the surface uplift velocity, which can go up to 2.4 cm/a for large connection zones (see figure 9E).

An additional advantage of our implementation is that it allows recomputing the effect of the overpressure in terms of an influx or an inflation volume. One can compute the influx volume by multiplying the boundary velocity, resulting from applying the overpressure, by the timespan of the inflation, or the timespan of high surface uplift velocities and retrieve the amount of the inflated magma. The area of applied overpressure in all simulations is 50 km^2. If one assumes an overpressure of 50 MPa, resulting in an average z-velocity of 23.4 cm/a at the boundary (approximately 3 cm/a within the plume), and timespan of high activity described by [52] from 2003 to 2008 the magma inflation volume is 0.06 km^3 at the mantle plume level after only 5 years.

6. Connections, visco-elasto-plastic, Influx chambers

The second scenario to add magma into the upper crustal chamber, is by taking it from partial melting or fractional crystallization of the lower crustal magma chamber. This implies that inflation in the upper magma chamber is accompanied by deflation in the lower chamber, which can be implemented numerically by introducing a connecting zone ('dike') between the two chambers in which a Poiseuille-flow (quadratic) velocity field is prescribed as an internal boundary condition. By varying the magnitude of the velocity we can control both the mass flux and the pressure gradient between the chambers. If only a connecting dike zone is present, the self

consistent (buoyant) velocity in the channel has an average value of 4.3 cm/a, which is equal to moving a volume of 0.006 km^3 between the chambers within 5 years. If we increase this velocity to an average of 8 cm/a, the surface velocities increase from 1.2 cm/a to 2 cm/a and the inflation volume to 0.012 km^3 (figure 5F). The volume of the applied velocity is 50 km^3 and the cross sectional area is 30 km^2. This thus has the largest impact on the surface velocities of all the scenarios we considered (see figure 9F for a summary).

D. Stress directions

Our models also compute stress orientations, which can be compared against available observations. In Yellowstone, [21] assembled the local stress orientation of the minimum principal stress σ_3 for selected locations by using earthquake focal mechanisms (white arrows in figure 1). Comparing modelled with observed principal stress directions reveals that there is a quite good agreement, particularly with respect to the stress orientation that changes from West-East to North-South (figure 6). Furthermore, both the connected and unconnected geometries have almost the same patterns, suggesting that both scenarios correlate well with the data.

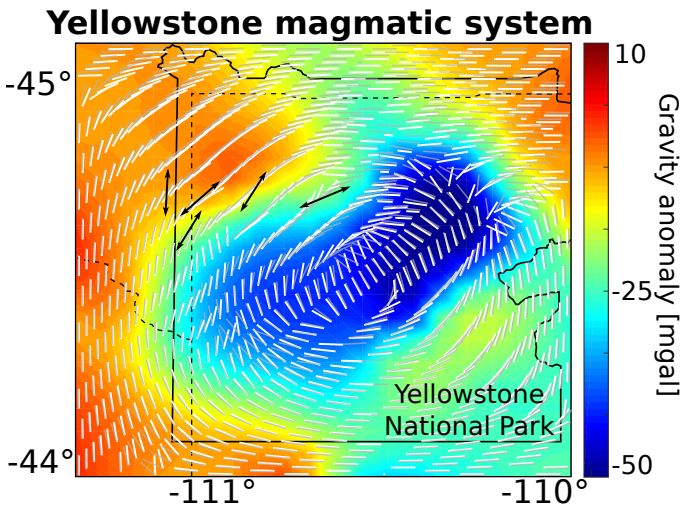

FIG. 6. Orientation of the minimum principal stress. Black arrows represent the orientation of the minimum principal stress taken from [21] and references therein. White arrows show the result of the simulation with no connection between the chambers, while grey arrows show the result of the simulation with connected chambers and a mantle plume (figure 5C). The stress orientation is computed at the surface. Results reproduce the rotation of the stress field from West-East to North-South. Furthermore, the connected versus the unconnected case do not show significant differences.

E. Parameter sensitivity

So far, we focused on how the connectivity between the chambers, the type of rheology and the inflation affect the surface velocity. However, in addition, material parameters such as the powerlaw exponent or the density will affect the dynamics of the system. We therefore perform a parameter sensitivity analysis, shown in figure 7, to determine the model parameters that play a key role in controlling the surface velocity. We compute these sensitivities for the representative simulation with visco-elasto-plastic rheology and connected chambers. Results are obtained for the cases in which we take the activation energy, the power law exponent and the density of the chambers into account, which amounts to 16 parameters in total. Of these, the viscosity parameters of the lower crust, as well as the density of the upper crust are the most important parameters as can be seen in figure 7. The size of the spheres in the figure visualize the normalized relative importance of the parameters. To enable direct comparison, each parameter type, e.g. activation energies, is normalized over the maximum parameter value within the type.

F. Adjoint inversion

In the next step we solve an inverse problem based on our 'best-scenario' model from previous section to obtain an improved fit between the simulations and observed GPS velocities. We allow the inversion to vary the activation energy and the power law exponent of the upper and lower crust, the asthenosphere and lithosphere. Figure 8A shows the viscosity field, which was used as initial guess. The final viscosity field has a significantly weakened crusts as a result of an increased power law exponent of the upper crust from 2.4 to 3 and from 3.2 to 4.6 for the lower crust (figure 8B). The inverse problem is solved by a steepest descent method and typically demonstrates a quick convergence, facilitated by a robust line-search algorithm (figure 8E).

A comparison between the modeled and observed velocity field between September 2007 and September 2008 (interpolated from data from [52]), shows that the pattern and magnitude are similar (figure 8C and D). This thus suggests that it is possible to fit the long-term or background surface velocities above magmatic systems by changing the viscosity structure of the crust. Smaller-scale differences that can be observed towards the boundaries, may occur because we consider the rheology of the crust to be homogeneous outside the magma chambers, whereas in nature weakening of the nearby surrounding crust may result from phases of inflation, heating, or deflation. In general, changing the viscosity structure only influences the long term surface velocities and stresses, and does not represent a short term signal like the inflation models discussed in section V C 5.

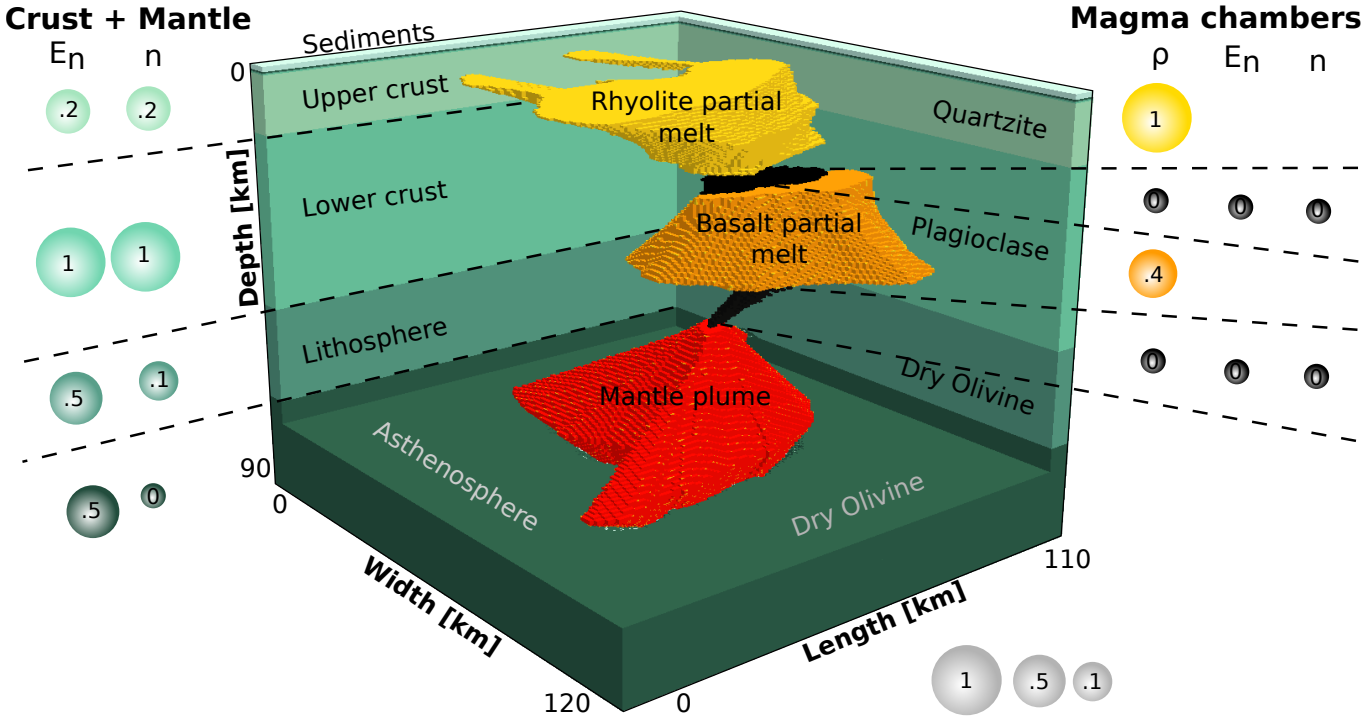

FIG. 7. Result of the adjoint parameter sensitivity study. The size of the sphere represents the relative importance of the parameter in affecting the surface velocity above the uppermost magma chamber. The viscosity of the lower crust, lithosphere and the lower crustal magma chamber together with the densities of the magma chambers are the key model parameters.

VI. DISCUSSION AND CONCLUSIONS

In this work, we present 3D visco-elasto-plastic numerical modeling of the lithospheric scale Yellowstone magmatic system. The geometry of our models is inspired by the recent seismic study of the area described in [1]. Additionally, the effective densities of the magma host rocks and the crust are obtained by thermodynamically consistent modeling using Perple_X [40] and the approach in [47].

In a first step, we show that it is important to consider 3D models instead of 2D ones, because the magnitudes (e.g., of velocities) can be very different. Next, we used gravity inversions to derive a reasonable density structure, which was subsequently used in a series of forward simulations in which we tested the effect of lithospheric rheology, chamber connectivity and magma influx on surface velocities. These simulations suggest that observed background uplift rates can be obtained for simulations in which the chambers are connected and plasticity is active in the upper crust. Velocity magnitudes obtained in this manner vary between 0.2 to 1.2 cm/a depending on whether plasticity is active or not, on the viscosity of the chambers, and on whether the chambers are connected, as shown in figure 9A and B.

We perform a comparison of the surface velocities with GPS measurements. [52] report phases of higher surface uplift rates during a timespan of one year between September 2007 and September 2008, representing velocities between 2 and 4 cm/a. To account for these enhanced velocities we considered two additional processes: (i) overpressure at the lower boundary of the domain to simulate magma rising from the mantle plume through the magmatic plumbing system, and (ii) magma transfer from the lower to the upper magma chamber, by applying a kinematic internal boundary condition between the two chambers at the location of the connection. The effect of overpressure appears to have a relatively minor impact on the surface velocities and most likely only contributes to the long term signal at the surface velocities. On the other hand, the prescribed Poiseuille flow between the upper and lower chambers has a much bigger effect. Increasing the magma flux between the chambers results in large changes of the surface velocities, e.g. 12 cm/a imposed velocity within the connection, which is equivalent to an inflation volume of 0.018 km^3 within only 5 years, nearly doubles the surface uplift velocity to 2.6 cm/a.

An adjoint-based sensitivity analysis is performed to demonstrate that the viscosity parameters of the upper and lower crust are of key importance for the surface velocities. An inversion was performed to better fit the models to both the magnitude and spatial pattern of the recorded uplift during a period of high activity with velocities of up to 4 cm/a [52]. Results show that this can be fitted with a weakened crust. Yet, changing the viscosity structure of the whole crust affects the long term up-

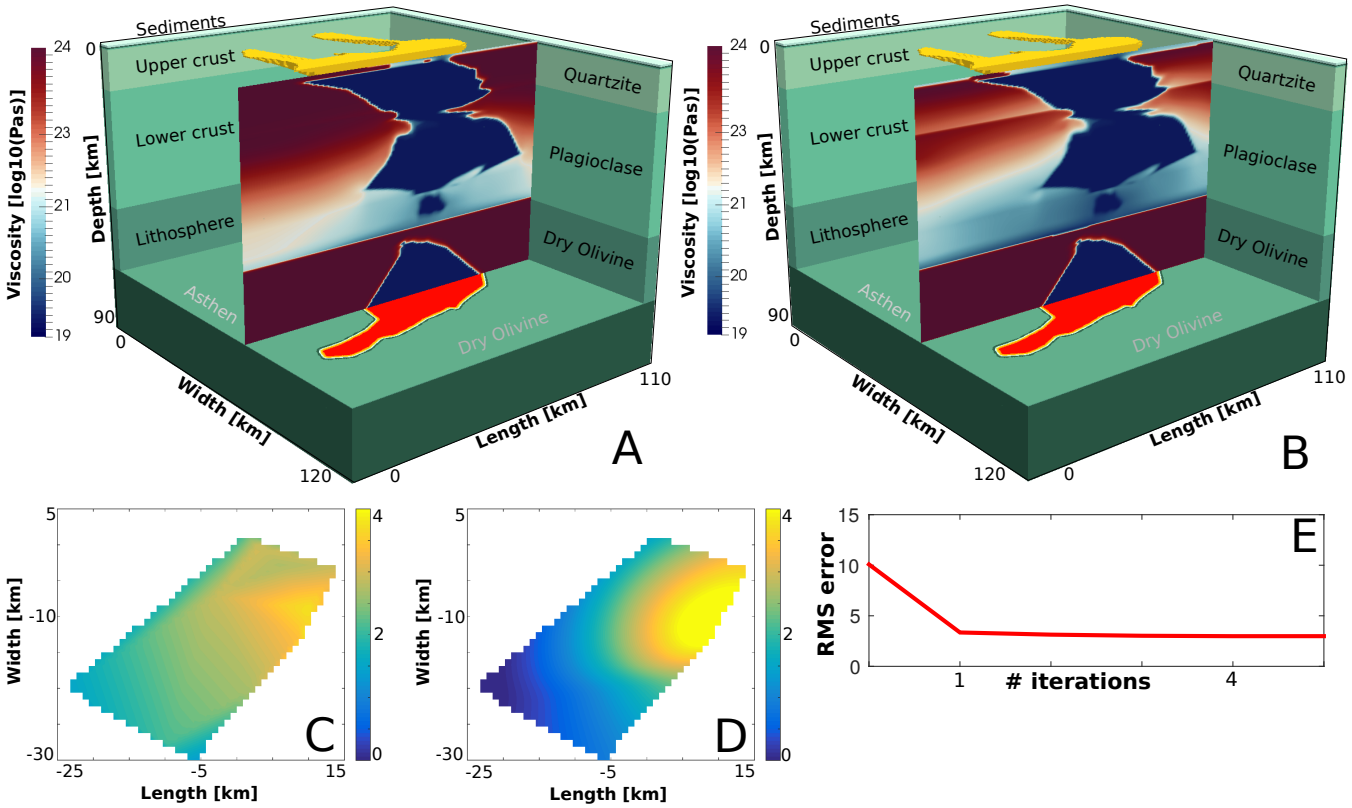

FIG. 8. Summary of the adjoint inversions for material parameters. A: Initial viscosity field of the visco-elasto-plastic connected case was (figure 5C) used as starting guess for the inversion. B: Final viscosity field after converged iterations, showing a significantly weakened crust by increasing the powerlaw exponents of the crust. C: Map view of interpolated surface uplift from [52] during the period of September 2007 to September 2008, which is used as data for our inversions. D: Map view of the vertical surface velocity field after converged iterations. Both the patterns and magnitude are similar, even though the numerical model has lower velocities towards the boundaries of the map, perhaps caused by crustal heterogeneities that were not taken into account in the models. E: Cost function as root mean square of vertical surface velocity versus number of iterations. Due to a good initial guess and robust line search acceleration, convergence is achieved quickly.

lift signal as well, while a short term period of enhanced uplift is more likely caused by a smaller scale magmatic pulse in the upper crust. In future work, it would thus be interesting to take the temporal evolution of the surface uplift signal into account (for example from INSAR data) as it may allow unraveling both the long term uplift, and the emplacement of a smaller scale magma pulses in a rheologically realistic lithosphere.

Other effects, that could potentially play an important role, and should ultimately be considered in these type of models, are: (i) deformation of a two- or three-phase mush, and (ii) volume changes resulting from crystallization [54]. Moreover, we can potentially increase the robustness of the inversions by taking more data into account, such as seismic activity as an estimation for the proximity to failure within the crust, or by directly inverting for stress orientations as well.

CONFLICT OF INTEREST STATEMENT

The authors declare that the research was conducted in the absence of any commercial or financial relationships that could be construed as a potential conflict of interest.

AUTHOR CONTRIBUTIONS

GR created the manuscript, created the Perple_X phase diagrams, temporarily implemented the gravity computation and the phase diagram feedback into LaMEM and performed all simulations presented in this work. BK proposed the main idea and helped in all aspects of this work as supervisor. AP is the main developer of LaMEM and helped with implementation issues. TB supported processing the raw gravity data, implementing the gravity solver into LaMEM and helped with interpreting inversion results. All authors contributed to the writing and statements made in this work.

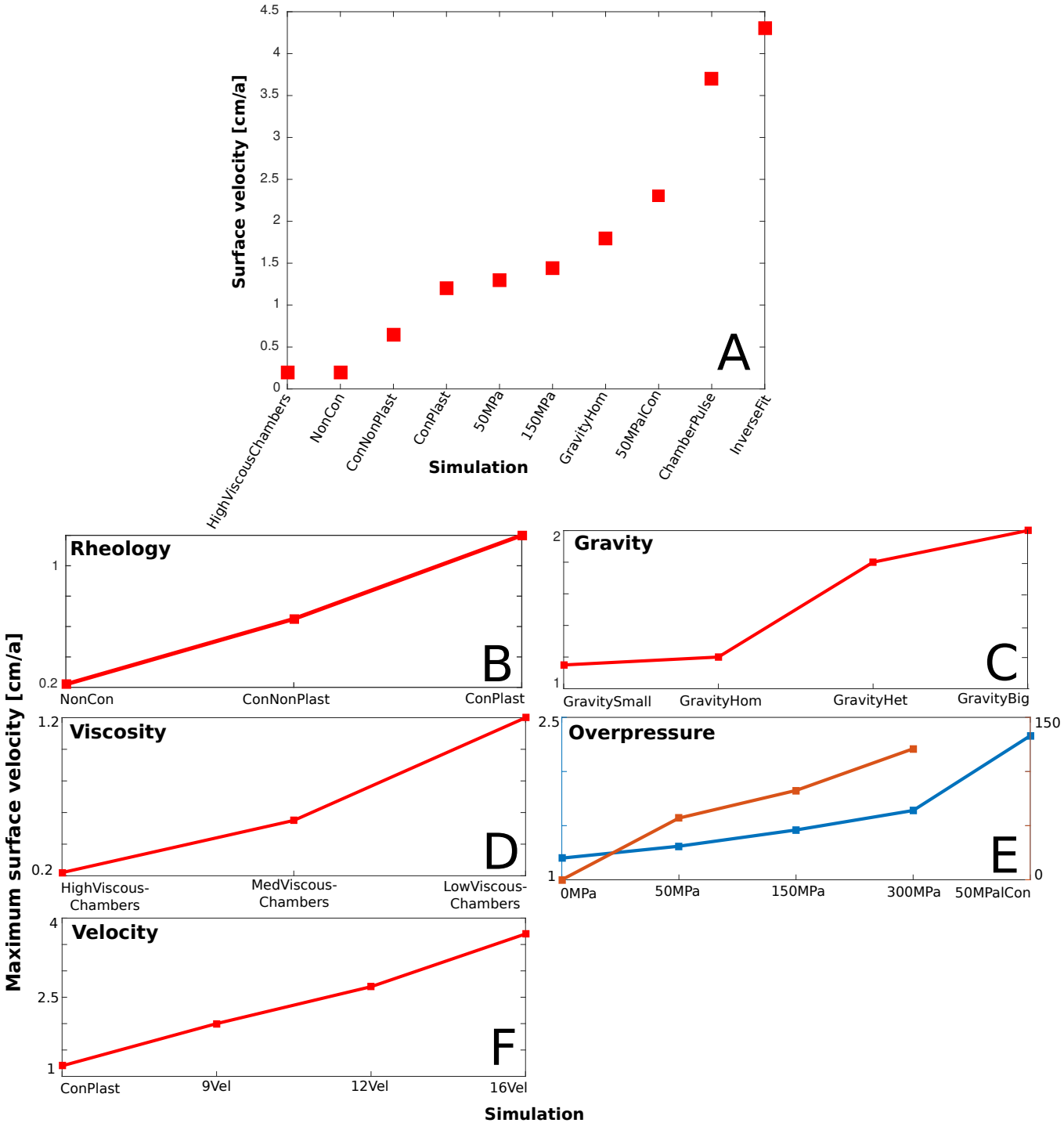

FIG. 9. Summary of the impact of the various parameters considered here on the vertical surface velocity. A: Set of representative simulations and the resulting surface velocities. B: Effect of rheology. C: Effect of the different density models on the surface velocity. D: Viscosity of the magma chambers. E: Effect of overpressure at the mantle plume. Blue curve represents the surface velocity. Red curve shows the maximum z-velocity at the boundary where the overpressure is applied (numbers on the right axis). F: Effect of kinematic internal boundary condition between the chambers simulating inflation and deflation between the upper and lower chambers, respectively. The largest effect on the vertical surface velocity is caused by changing the kinematic boundary condition.

Abbreviations: NonCon: No connection between chambers and visco-elastic rheology. ConNonPlast: Connected chambers with visco-elastic rheologies. ConPlast: Connected chambers with visco-elasto-plastic rheologies. GravitySmall: 10 % smaller chambers, homogeneous density. GravityHom: Homogeneous density strucutre as used in the rest of the work. GravityHet: Heterogeneous density field fitted by hand. GravityBig: 10 % larger chambers, homogeneous density. HighViscousChambers: Viscosity of chambers 1e21. MedViscousChambers: Viscosity of chambers 1e20. LowViscousChambers: Viscosity of chambers 1e19. 0MPa: no overpressure applied at the mantle plume. 50MPa: 50 MPa overpressure at the mantle plume. 150MPa: 150 MPa of overpressure at the mantle plume. 300MPa: 300 MPa overpressure at the mantle plume. 50MPalCon: 50 MPa at the mantle plume and larger connections between the chambers which increases the effect of pressure propagation through the domain. InverseStart: Starting guess of the inversion as shown in figure 8A. InverseSmallStep: Converged inverse result using a small step size. InverseFit: Result after converged inversion with larger step size as shown in figure 8B. 9Vel: Artificially increased maximum velocity in the channel to 9 cm/a. 12Vel: Artificially maximum increased velocity in the channel to 12 cm/a. 16Vel: Artificially increased maximum velocity in the channel to 16 cm/a.

FUNDING

GR received funding from the University of Mainz.

ACKNOWLEDGMENTS

We would like to thank the ZDV at the University of Mainz to provide us computational time on MOGON I and MOGON II cluster.

[1] H.-H. Huang, F.-C. Lin, B. Schmandt, J. Farrell, R. B. Smith, and V. C. Tsai, Science **348**, 773 (2015).
[2] K. V. Cashman, R. S. J. Sparks, and J. D. Blundy, Science **355**, eaag3055 (2017).
[3] K. Mogi, Earthquake research institute **36**, 99 (1958).
[4] R. Lanari, P. Lundgren, and E. Sansosti, Geophysical Research Letters **25**, 1541 (1998).
[5] E. Kjartansson and K. Gronvold, Nature **301**, 139 (1983).
[6] S. Hautmann, J. Gottsmann, R. S. J. Sparks, A. Costa, O. Melnik, and B. Voight, Tectonophysics **471**, 87 (2009).
[7] E. Trasatti, C. Giunchi, and M. Bonafede, Journal of Volcanology and Geothermal Research **122**, 89 (2003).
[8] A. Manconi, T. R. Walter, M. Manzo, G. Zeni, P. Tizzani, E. Sansosti, and R. Lanari, Journal of Geophysical Research: Solid Earth **115** (2010).
[9] C. Del Negro, G. Currenti, and D. Scandura, Physics of the Earth and Planetary Interiors **172**, 299 (2009).
[10] G. Currenti, A. Bonaccorso, C. Del Negro, D. Scandura, and E. Boschi, Earth and Planetary Science Letters **296**, 311 (2010).
[11] M. Gerbault, F. Cappa, and R. Hassani, Geochemistry, Geophysics, Geosystems **13** (2012).
[12] P. Davis, L. Hastie, and F. Stacey, Tectonophysics **22**, 355 (1974).
[13] M. Battaglia and P. Segall, Geodetic and Geophysical Effects Associated with Seismic and Volcanic Hazards , 1453 (2004).
[14] W. Degruyter and C. Huber, Earth and Planetary Science Letters **403**, 117 (2014).
[15] C. Annen, J.-F. Lénat, and A. Provost, Journal of Volcanology and Geothermal Research **105**, 263 (2001).
[16] C. Annen and R. S. J. Sparks, Earth and Planetary Science Letters **203**, 937 (2002).
[17] L. Karlstrom, S. R. Paterson, and A. M. Jellinek, Nature Geoscience **20**, 177 (2017).
[18] M. Paulatto, C. Annen, T. J. Henstock, E. Kiddle, T. A. Minshull, R. Sparks, and B. Voight, Geochemistry, Geophysics, Geosystems **13** (2012).
[19] R. L. Christiansen, *The Quaternary and pliocene Yellowstone plateau volcanic field of Wyoming, Idaho, and Montana*, Tech. Rep. (U.S. Geological Survey, 2001).
[20] D. Vasco, C. Puskas, R. Smith, and C. Meertens, Journal of Geophysical Research: Solid Earth **112** (2007).
[21] G. P. Waite and R. B. Smith, Journal of Geophysical Research: Solid Earth **109** (2004).
[22] R. B. Smith and L. W. Braile, Journal of Volcanology and Geothermal Research **61**, 121 (1994).
[23] R. B. Smith, M. Jordan, B. Steinberger, C. M. Puskas, J. Farrell, G. P. Waite, S. Husen, W.-L. Chang, and R. O'Connell, Journal of Volcanology and Geothermal Research **188**, 26 (2009).
[24] T. S. Baumann, B. J. Kaus, and A. A. Popov, Tectonophysics **631**, 197 (2014).
[25] T. S. Baumann and B. J. Kaus, Geophysical Journal International **202**, 1289 (2015).
[26] V. Ratnaswamy, G. Stadler, and M. Gurnis, Geophysical Journal International **202**, 768 (2015).
[27] B. Kaus, A. Popov, T. Baumann, A. Pusok, A. Bauville, N. Fernandez, and M. Collignon, in *NIC Proceedings*, Vol. 48, edited by K. Binder, M. Mller, M. Kremer, and A. Schnurpfeil (2016) pp. 299–307.
[28] M. Kameyama, D. Yuen, and S. Karato, Earth and Planetary Sciences Letters **168**, 159 (1999).
[29] D. C. Drucker and W. Prager, Quarterly of applied mathematics **10**, 157 (1952).
[30] F. Harlow and J. Welsh, Phys. Fluids **8**, 2182 (1965).
[31] T. V. Gerya and D. A. Yuen, Physics of the Earth and Planetary Interiors **163**, 83 (2007).
[32] P. J. Tackley, Physics of the Earth and Planetary Interiors **171**, 7 (2008).
[33] B. J. Kaus, H. Mühlhaus, and D. A. May, Physics of the Earth and Planetary Interiors **181**, 12 (2010).
[34] T. Duretz, D. A. May, T. V. Gerya, and P. J. Tackley, Geochemistry, Geophysics, Geosystems **12** (2011), 10.1029/2011GC003567.
[35] S. Balay, S. Abhyankar, M. F. Adams, J. Brown, P. Brune, K. Buschelman, L. Dalcin, V. Eijkhout, W. D. Gropp, D. Kaushik, M. G. Knepley, L. C. McInnes, K. Rupp, B. F. Smith, S. Zampini, H. Zhang, and H. Zhang, *PETSc Users Manual*, Tech. Rep. ANL-95/11 - Revision 3.7 (Argonne National Laboratory, 2016).
[36] D. Plouff, Geophysics **41**, 727 (1976).
[37] D. L. Turcotte and G. Schubert, *Geodynamics* (Cambridge University Press, 2014).
[38] A. Ismail-Zadeh, A. Korotkii, B. Naimark, and I. Tsepelev, Computational mathematics and mathematical physics **43**, 581 (2003).
[39] G. S. Reuber, A. A. Popov, and B. J. Kaus, Tectonophysics (2017).
[40] J. Connolly, Geochemistry, Geophysics, Geosystems **10** (2009).
[41] C. Baumann, T. V. Gerya, and J. A. Connolly, Geological Society, London, Special Publications **332**, 99 (2010).
[42] S. Angiboust, S. Wolf, E. Burov, P. Agard, and P. Yamato, Earth and Planetary Science Letters **357**, 238 (2012).

[43] A. Koptev, E. Burov, E. Calais, S. Leroy, T. Gerya, L. Guillou-Frottier, and S. Cloetingh, Geoscience Frontiers **7**, 221 (2016).
[44] A. Koptev, E. Burov, T. Gerya, L. Le Pourhiet, S. Leroy, E. Calais, and L. Jolivet, Tectonophysics (2017).
[45] T. Holland and R. Powell, Journal of metamorphic Geology **16**, 309 (1998).
[46] R. Rudnick and S. Gao, Treatise on geochemistry **3**, 659 (2003).
[47] Y. Bottinga and D. F. Weill, American Journal of Science **269**, 169 (1970).
[48] T. S. Baumann and A. Bauville, in *EGU General Assembly Conference Abstracts*, Vol. 18 (2016) p. 17980.
[49] F. Crameri, H. Schmeling, G. Golabek, T. Duretz, R. Orendt, S. Buiter, D. May, B. Kaus, T. Gerya, and P. Tackley, Geophysical Journal International **189**, 38 (2012).
[50] K. R. DeNosaquo, R. B. Smith, and A. R. Lowry, Journal of Volcanology and Geothermal Research **188**, 108 (2009).
[51] W.-L. Chang, R. B. Smith, C. Wicks, J. M. Farrell, and C. M. Puskas, Science **318**, 952 (2007).
[52] W.-L. Chang, R. B. Smith, J. Farrell, and C. M. Puskas, Geophysical Research Letters **37** (2010).
[53] M. E. Reid, Geology **32**, 373 (2004).
[54] R. O. Fournier, Annual Review of Earth and Planetary Sciences **17**, 13 (1989).
[55] G. Ranalli, *Rheology of the Earth* (Springer, 1995).
[56] Y. Saad, SIAM Journal on Scientific Computing **14**, 461 (1993).
[57] J. Hickey and J. Gottsmann, Journal of Volcanology and Geothermal Research **280**, 126 (2014).
[58] U. Ayachit, (2015).

Appendix A: Numerical performance

The simulations presented in this work are performed with LaMEM, which is available as open source code from https://bitbucket.org/bkaus/lamem (see [27]). LaMEM relies on the PETSc framework, which allows running it on a variety of machines from laptops to massively parallel clusters [35]. The simulations reported here have been performed on 128 cores with around 1Gb memory/core. We employed the preconditioned Jacobian-Free Newton-Krylov method together with the FGMRES [56] iterative solver, combined with a multigrid preconditioner to approximately invert the Stokes block in the preconditioning matrix using Galerkin coarsening. We implemented custom restriction and prolongation operators that suit the multigrid framework within PETSc for a staggered grid finite difference discretization. This multigrid preconditioner was configured with 4 levels using V-cycles. A maximum of 20 nonlinear Newton iterations are allowed. If the relative change in the residual is more than 10^{-6} the iteration is assumed to have converged.

Appendix B: Elastic stress build-up

As we are interested in the steady-state evolution of the lithosphere and magmatic system, which formed over millions of years, we cannot simply start the model with zero initial stresses and directly interpret the results. This is because visco-elastic effects will increase stresses with time until a saturation effect is reached. Using a visco-plastic rheology, as is often done in geodynamic models, is also not appropriate as this would not allow simulating the effect of injecting magma into the upper chambers.

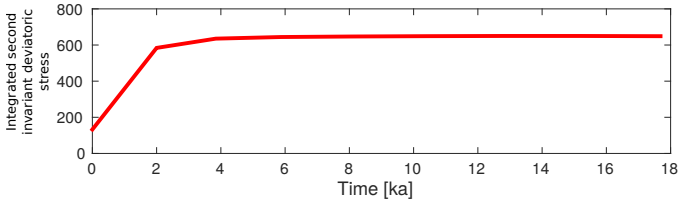

FIG. 10. Integrated second invariant of the deviatoric stress tensor versus time over a small area within the domain. Integration is done to capture a representative volume and not only a single point. After 5 ka no change in stresses can be observed.

We therefore include elasticity and performed tests to see how many time steps are required to reach a steady-state stress within the lithosphere, such that subsequent results are not affected by this stress initialization stage. For the parameters reported here, running the simulations for a certain time interval, around 10 ka, is sufficient as after that both stresses and velocities saturate. The comparison of the resulting surface velocities with data is only performed after this stage. Figure 10 shows volume-averaged integral of the second invariant of the deviatoric stress tensor versus time, indicating that after 5 ka the stresses stop changing.

Appendix C: Mogi analytical solution benchmark

[3] developed a widely used analytical solution and benchmark that describes the inflation of a sphere in an elastic half-space. [9] extended this solution and derived the surface displacements over an inflated sphere in a visco-elastic halfspace. A summary of available benchmarks and example cases can be found in [57]. As this type of problems has not been tested with LaMEM before, we verify the code by reproducing the visco-elastic Del Negro benchmark. The setup has a width and length of 30 km and a depth of 5 km, with a magma source in the middle of the domain that has a radius of 1 km and is overpressurized by 10 MPa. The shear modulus is 4 GPa and the corresponding Poisson ratio 0.25. The magma source has a viscosity of 10^5 Pas and the surrounding rocks have 10^{17} Pas. The result is taken after a model evolution of 1 year. The results are shown in figure 11, and show that good agreement exists between the two approaches.

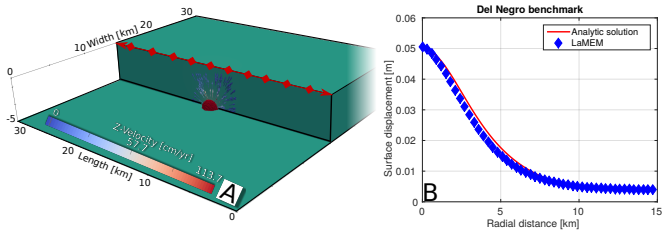

FIG. 11. Comparison of analytical [9] versus numerical results. A: Setup used for the benchmark. Red sphere in the middle of the domain represents the magma source with an overpressure of 10 MPa. Arrows indicate velocities. B: Comparison between analytical solution (red line) and the result of LaMEM (blue line) as surface displacement versus radial distance to the source, along the red line in A.

Appendix D: Simulation animation

The pathway of the material within the magma chambers can be visualized in a movie by tracking passive markers through the velocity field. We use the 'Streaming Lines Representation' tool of the freely available visualization application Paraview [58]. The model presented in the movie is the one discussed in section V C 3. In the movie one can see the acceleration of the fluid within the channel and the uplift velocity at the surface. Furthermore, the velocities are maximum close to the channels or in the middle of the chambers while the corner areas

show small velocities. At the western wall of the domain the viscosity structure is shown. The movie is given in the online supplemental material.